Journal of Fluids and Structures 27 (2011) 1349–1356

Contents lists available at ScienceDirect

Journal of Fluids and Structures

journal homepage: www.elsevier.com/locate/jfs

Dynamics of the flow around colliding spheres

Martin D. Griffith [a,*], Lionel Schouveiler [b], Mark C. Thompson [a], Kerry Hourigan [a]

[a] Fluids Laboratory for Aeronautical and Industrial Research (FLAIR), Department of Mechanical and Aerospace Engineering & Division of Biological Engineering, Monash University, Melbourne, Victoria 3800, Australia

[b] Institut de Recherche sur les Phénomènes Hors Equilibre (IRPHE), CNRS/Aix-Marseille Université, 49 rue Frédéric Joliot-Curie, BP 146, F-13384 Marseille Cedex 13, France

ARTICLE INFO

Article history:
Received 2 December 2010
Accepted 20 May 2011
Available online 12 June 2011

Keywords:
Vorticity dynamics
Particle impact

ABSTRACT

An investigation of the flow resulting from the collision of two spheres at low Reynolds numbers is presented. Each sphere starts from rest and traverses a distance of 5 sphere diameters to the point of contact. Experimental and numerical results are compared for a symmetric collision; that is, a collision between two spheres of the same diameter and travelling with the same velocity. The flow consists of two axisymmetric recirculation zones which become a pair of colliding vortex rings, expanding radially from the collision point. Several examples of unbalanced collisions are also presented numerically, with one or both of the velocity and diameter of the spheres altered. These collisions break the symmetry, altering the post-collision expansion of the vortex rings.

Several studies have investigated the dynamics of particle–particle and particle–wall collisions, often presented in the context of solid–liquid flows. In particle–particle collisions, Davis et al. (1986) investigated the elastic particle deformation arising from fluid pressure and its effect on rebound. Similarly, Yang and Hunt (2006) characterized the post-collision motion of two spheres by a coefficient of restitution and a friction coefficient. Joseph et al. (2001) explored the rebound and restitution properties of particle–wall collisions for Reynolds numbers up to 3000. The resulting flow consisted of a recirculating zone moving from behind the particle, expanding, and then sitting on the wall.

The behaviour of the post-collision flow of a particle–wall impact can cause a re-suspension of dust particles. Eames and Dalziel (2000) experimentally explored the hydrodynamic mechanism for dust re-suspension, characterizing the behaviour by different dust volume concentrations. Turning more to the fluid dynamical aspects of the problem, Leweke et al. (2006, 2008) and Thompson et al. (2007) examined the behaviour of the post-collision flow. They found that the vorticity dynamics bear much similarity to the collision of a vortex ring with a wall, an interaction which has been investigated by a number of researchers, including Walker et al. (1987), Orlandi and Verzicco (1993) and Munro et al. (2009).

In the present work, we focus on the post-collision fluid dynamics of sphere–sphere collisions. The focus is on a simplified set-up consisting of an abrupt inelastic collision without rebound; this will form the basis for work on more complex models incorporating further parameters, such as deceleration and sphere rebound. If the flow dynamics of a sphere–wall collision bear similarity to the collision of a vortex ring with a wall, we may expect a similarity between the flow dynamics of sphere–sphere collisions and those of the collision of two vortex rings.

The first part of the paper looks at symmetric collisions between two spheres, where the spheres are of the same size and traveling with the same speed. The second part of the paper looks at unbalanced collisions, where one of, or both of, the velocity and diameter of the two spheres are not matched.

* Corresponding author.
E-mail address: martin.griffith@eng.monash.edu.au (M.D. Griffith).

0889-9746/$ - see front matter © 2011 Elsevier Ltd. All rights reserved.
doi:10.1016/j.jfluidstructs.2011.05.003

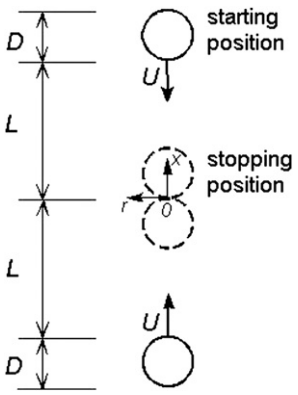

Fig. 1. Parameters and geometry of a sphere–sphere collision.

1. Problem definition

We first consider symmetric collisions for which the system consists of two equal spheres of diameter D and approaching each other with the same, but opposite, constant velocity U (see the sketch in Fig. 1). The two spheres are initially at rest at a distance of $2L$, one from the other. Both spheres are impulsively started and travel a distance L at the velocity U, with the trajectory of the two centres on the same line. The spheres are then impulsively stopped at the moment of contact.

The principal control parameters of the problem are the non-dimensional running distance L/D and the Reynolds number $\mathrm{Re} = UD/\nu$, where ν is the kinematic viscosity of the fluid. Time, τ, is non-dimensionalized using the advection time D/U, with the impact of the spheres occurring at $\tau = 0$. The coordinates x and r are non-dimensionalized using D (Fig. 1), with the origin at the contact point of the two spheres and the x axis corresponding to the sphere centre trajectories. The second part of the study explores asymmetric collisions that require the definition of parameters for each sphere. Thus, we define Re_t as the Reynolds number based on the velocity and diameter of the upper sphere in our images, while Re_b refers to the lower. We also define velocity and diameter ratios, U_t/U_b and D_t/D_b. With these definitions the balanced symmetric collisions correspond to $U_t/U_b = D_t/D_b = \mathrm{Re}_t/\mathrm{Re}_b = 1$. For the investigation of asymmetric collisions, we have considered, first, cases where Re_t is reduced by altering either the velocity or diameter ratios and, second, a case where the velocity and diameter ratios are not equal to one, but are balanced such that $\mathrm{Re}_t/\mathrm{Re}_b = 1$. For all cases, note that the running distance L/D for each sphere is calculated independently, based on the corresponding sphere diameter.

2. Method

Experimentally, the flow was examined in a 600 mm high glass tank, of $500 \times 500\ \mathrm{mm}^2$ horizontal cross-section, filled with water. Two brass spheres of diameter $D = 19.02$ mm were used. Each sphere was hung at the end of an inelastic thread. The thread of the lower sphere passed through a hole drilled along the vertical diameter of the upper sphere and was wrapped around a reel. The thread of the upper sphere was wrapped around an identical reel but in the opposite direction. The two reels were mounted on the same horizontal axis situated above the tank parallel to the free surface. The axis was driven in rotation by a high resolution computer-controlled stepper motor. With such a setup, the rotation of the driven axis induced vertical translations of the two sphere centres along the same axis and at the same velocity, but in opposite directions.

Experimental investigation was based on coloured dye visualization. The two spheres were initially coated with a solution of fluorescent dye. They were set at their starting positions, and lowered together slowly into the water, before running the experiment.

The dye pattern created by the flow entrainment was illuminated from the side with a vertical sheet of laser light containing the sphere centres. A mirror was placed on the opposite side to reflect the laser sheet and illuminate the area in the shadow of the spheres. The flow was recorded through the tank wall with a video camera operating at 25 frames per second and placed perpendicular to the laser sheet. The CCD sensor was of 768×576 pixels, resulting, for the fields visualized in the present study, in a space resolution of $D/82 = 0.23$ mm/pixel.

Numerically, an in-house spectral-element solver, employing an arbitrary Lagrangian-Eulerian (ALE) method (Hirt et al., 1974) to handle the moving boundaries, was used to numerically simulate the flow. The same solver has previously been successful in modeling the touchdown of a sphere against a wall (Thompson et al., 2007), so only a brief summary of the method is given here. Due to the symmetry of the problem, simulations could have been run with a free boundary at the collision point; however, both sides of the collision have been simulated in order, first, to emphasize this symmetry with respect to the plane $x = 0$ and, second, to enable the simulation of non-symmetric collisions. As each simulation progresses and the spheres move closer to each other, the vertices of the computational mesh move at specified predetermined

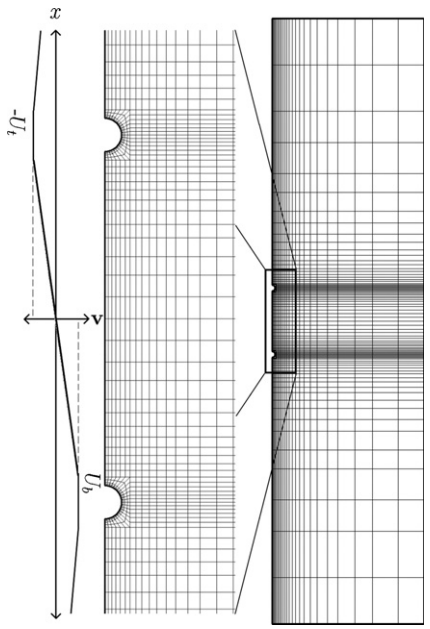

Fig. 2. At left: a plot of the scaled mesh velocity, which corresponds with the zoomed in view of the mesh. At right: the mesh over the entire computational domain is shown. Note: only macro-elements are shown.

velocities, which maintain the volume of the domain and the shape of the spheres. On the moving mesh, the velocity field satisfies the Navier–Stokes equations in addition to the incompressibility condition:

$$\frac{\partial \overline{\mathbf{u}}}{\partial t} + (\overline{\mathbf{u}} - \mathbf{v}) \cdot \nabla \overline{\mathbf{u}} = -\nabla \overline{p} + \nu \nabla^2 \overline{\mathbf{u}}, \tag{1}$$

$$\overline{\nabla} \cdot \overline{\mathbf{u}} = 0, \tag{2}$$

where $\overline{p}$ is the kinematic pressure, $\overline{\mathbf{u}}$ is the fluid velocity, $\mathbf{v}$ is the spatially varying mesh velocity and ν is the kinematic viscosity. Fig. 2 shows the computational mesh as well as a plot of the moving mesh velocity.

In the direction of the sphere translation, from one end of the domain, the mesh velocity varies linearly from zero to U on the mesh points on or near the sphere, and then varies again linearly to zero at $x=0$, the point of collision. From their starting positions at $x = \pm L/D$, to the collision, the simulation needed to be remeshed three or four times, to avoid excessive element distortion. After each interpolation, the original simulation was run slightly longer to overlap with the next part of the simulation, in order to check for any error caused by the re-meshing. Within the overlapped simulation time, parameters such as the viscous and pressure force acting on the spheres on the new mesh were found to be within one percent of those for the same time on the previous mesh.

In the numerical simulations, the spheres were stopped shortly before collision, in order to avoid a singularity of the mesh configuration at the point of contact between the spheres. The spheres were stopped with a gap of $0.01D$ between. Comparisons between experiments and numerical simulations presented below show that the small discrepancy in contact distance is negligible with respect to the evolution of the resulting flow. The domain extends $50D$ axially from the collision points, and $25D$ radially. Grid independence was tested by increasing the macro-element internal resolution. The internal node points are distributed according to Gauss–Legendre–Lobatto quadrature points; the resolution of the solution can be increased by incrementing the polynomial order of the quadrature. After running several test cases with an increased resolution of 49 ($n=7$) nodes per element (the presented results use 36 ($n=6$) nodes per element), no significant effect (greater than one percent) was observable in the behaviour of the viscous and pressure forces.

3. Results

In the present study, we focus on moderate Reynolds number, $100 \leq \mathrm{Re} \leq 800$, and on axisymmetric flows at the time of impact $\tau = 0$. To satisfy the latter condition, the running distance L/D is short enough for the wake to remain axisymmetric, but at the same time large enough to have a well-defined recirculation region behind each sphere. It has been checked that these two conditions are met for $L/D=5$ for all the tested values of Re. Moreover, for values of Re up to 800, it was observed that the flow after impact remains axisymmetric (three dimensional structures have been seen to develop for $\mathrm{Re} > 900$ in experiments and simulations of sphere impact on a wall (Leweke et al., 2004; Thompson et al., 2007)). Hence the depiction of only half of the experimental dye visualization in Fig. 3, which shows a sequence of images at different times of the flow

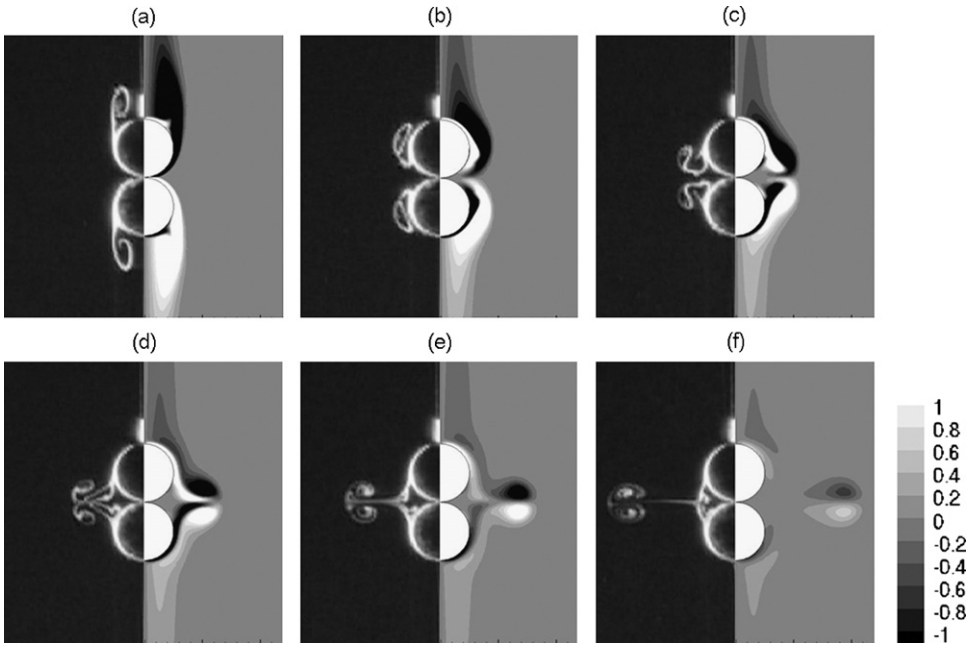

Fig. 3. Comparison of experimental dye visualizations (left) and numerical vorticity contours (right) for a sphere–sphere collision at Re=400, $L/D=5$ and at different times $\tau=0$ (a), 1 (b), 2 (c), 3 (d), 5 (e) and 10 (f) (10 contour levels $-1U/D \le \omega_\theta \le 1U/D$).

generated by a symmetric collision for Re=400, $L/D=5$. In comparison to the dye visualization, vorticity contours for the corresponding numerical simulation are shown.

Before the impact, the vorticity generated by the translation of the spheres rolls up in the wake of each sphere. At the time of impact (Fig. 3(a)) the flow consists of a vortex ring attached behind each sphere. Due to the inertia of the fluid, the two vortex rings continue to travel parallel to the x axis after the impact. As the two vortex rings pass over the spheres, secondary vorticity of opposite sign to that of the primary vortices is induced at the surface, as seen in Fig. 3(b) and (c). The secondary vorticity is stretched by the primary vortex (Fig. 3(d)) then quickly spreads due to the viscous diffusion, in such a way that at the subsequent instants only remnants of the secondary vorticity are still clearly visible in Fig. 3(e) and (f). Simultaneously, the primary vortex rings continue to travel towards each other then collide, in Fig. 3(d). As is well known for such a situation (for a review on head-on collisions of vortex rings see Shariff and Leonard (1992)), their interaction after collision leads to a growth of their diameter. The resulting radial motion of the vortex ring cross-sections can be observed in Fig. 3(e) and (f).

Similar behaviour is observed in all cases across the range of Reynolds numbers investigated, $100 < \mathrm{Re} < 800$, both experimentally and numerically. In particular, for all cases we note an up-and-down symmetry in the different views that is indicative of two identical vortex rings; that is, each vortex ring corresponds to the image of the other with respect to the $x=0$ plane.

Moreover, comparisons in Fig. 3 reveal a close qualitative match between numerical and experimental results. This allows us to validate both our numerical approach and the visualization technique to mark the vorticity at least for $\tau \le 10$. The suitability of the dye in representing the vorticity is limited by the difference between the diffusion coefficients of the dye and of the vorticity; this limit has previously been estimated to be $\tau \approx 20$ (Thompson et al., 2007). In the present study we have considered experimental results from visualizations only for $\tau \le 10$.

To discuss the effects of Reynolds number, Fig. 4 plots the trajectories of the primary vortex ring centres for various Re; due to the symmetries of the flow, we plot only trajectories of one primary vortex center in half of a meridional plane. The trajectories of the vortex ring centres predicted by the numerical simulations for different Reynolds numbers are plotted in Fig. 4(a) for $2 \le \tau \le 46$ ($2 \le \tau \le 14$ for Re=100 because of the fast diffusion of vorticity in this case) and compared to the trajectories obtained from following the centre of the dye spiral on visualizations for Re=200, 400, 800 plotted for τ from -1.2 (before the impact) to 10. The centre of the vortex ring is determined by visual inspection of the image. While this method is not entirely objective, a good match exists nonetheless between the experimental points and the numerical trajectories. Plotting only the radial coordinate as function of time in Fig. 4(b), we note that experimental points are above the numerical curves at low Re. Some difference in the two sets of results is to be expected: firstly, the coefficients of diffusion of the vorticity and the dye are different; and secondly, the centre of the recirculating dye is assumed to represent the centre of the vortex.

In addition, Fig. 4(b) shows that the radial growth of the vortex ring decelerates with time. At the time of impact, the vortex ring radius is approximately equal to the sphere radius $0.5D$ and extends to a limit value that depends on the

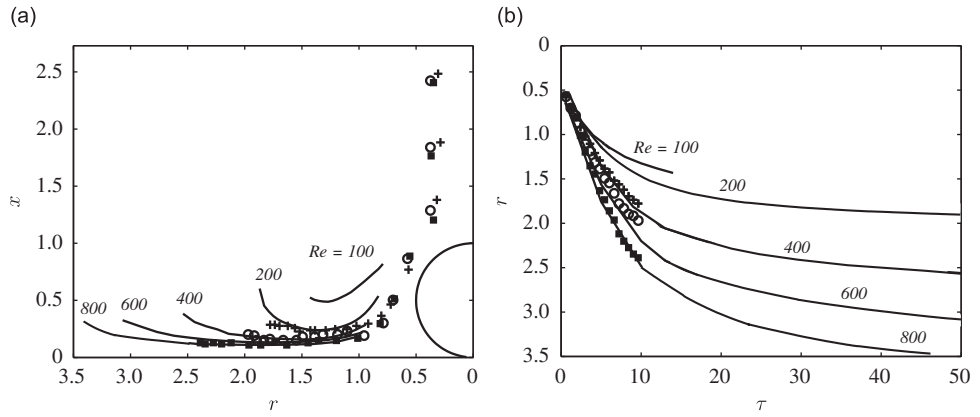

Fig. 4. (a) Trajectories of the primary vortex ring centres as obtained from the numerical simulations (for various Re) and from the experimental visualizations for Re=200 (+), 400 (○), 800 (■), and (b) the variation with time of the radial coordinate of these trajectories.

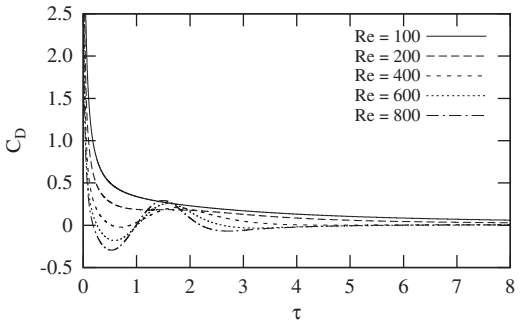

Fig. 5. Plots of drag force on the spheres as a function of time after collision.

Reynolds number. From the numerical results of Fig. 4(b), the vortex ring is seen to evolve from $2D$ for Re=200 to $3.5D$ for Re=800. This result differs from the case of a sphere impacting a wall (Thompson et al., 2007) where the radius of the vortex ring is always less than $1.5D$ for $\mathrm{Re} \leq 800$; the viscous effect on the solid wall is likely to contribute towards this particular difference between the two cases.

From the numerical data, Fig. 5 plots the non-dimensional drag coefficient of each sphere immediately after impact. For each case, the drag decreases quickly from its value at impact. At low Reynolds numbers, the drag converges slowly to zero as the flow around the spheres subsides. However, at higher Reynolds numbers, an oscillation in the drag force causes a negative drag for a short time, forcing the spheres together. In a more physically realistic simulation, this may have implications for the post-collision velocity of the spheres rebound that would occur. The oscillation is more pronounced at higher Reynolds numbers.

We have considered, experimentally and numerically, collisions of identical spheres, approaching along the same axis with the same (but opposite) velocity and running distance. The resulting flow consists of two identical colliding axisymmetric vortex rings, while also retaining a symmetry around the plane $x=0$. Numerical simulations have also been performed for asymmetric cases where the velocity and diameter of one of the spheres is varied. It is then necessary to define the velocity, the diameter and the resulting Reynolds number for the top and bottom sphere, referred to as U_t, D_t, $\mathrm{Re}_t = U_t D_t/\nu$ and U_b, D_b, $\mathrm{Re}_b = U_b D_b/\nu$, respectively. For all the simulations, the running distance of each sphere is maintained to five times its diameter ($L_t/D_t = L_b/D_b = 5$). Note, this normally requires one sphere to begin on its trajectory before the other. With the fixed running distances, the parameters of the system are the Reynolds numbers Re_t, Re_b and the velocity and diameter ratios U_t/U_b and D_t/D_b.

We first discuss results of numerical simulations conducted for two equally sized spheres ($D_t = D_b$) with $\mathrm{Re}_b = 400$ and four lower values for Re_t. Fig. 6 plots vorticity contours at four time instants after collision, where the velocity of the top sphere (i.e. the uppermost in the images) has been reduced, with Reynolds number ratios of $\mathrm{Re}_t/\mathrm{Re}_b = U_t/U_b = 0.9$, 0.8, 0.7 and 0.6. The resulting flow no longer possesses the symmetry with respect to the plane $x=0$ observed for the symmetric collision in Fig. 3 (the axisymmetry around the x axis is enforced numerically for all cases). Here, we need to consider the effect on the post-collision flow of the difference in the amount of circulation generated by each of the spheres, from the start of their trajectory to the end. Vorticity generated by the motion of the spheres will advect into the recirculation zone behind each sphere at the rate of $0.5U^2$ (Morton, 1984). Therefore, we expect that the amount of circulation in each vortex ring at the instant of impact will scale with $0.5U^2$ multiplied by the running time, or $0.5U^2L/U$. Therefore, for the case with $U_t/U_b = 0.8$, the slower traveling sphere generates 0.8 of the circulation of the faster one. After the impact, the

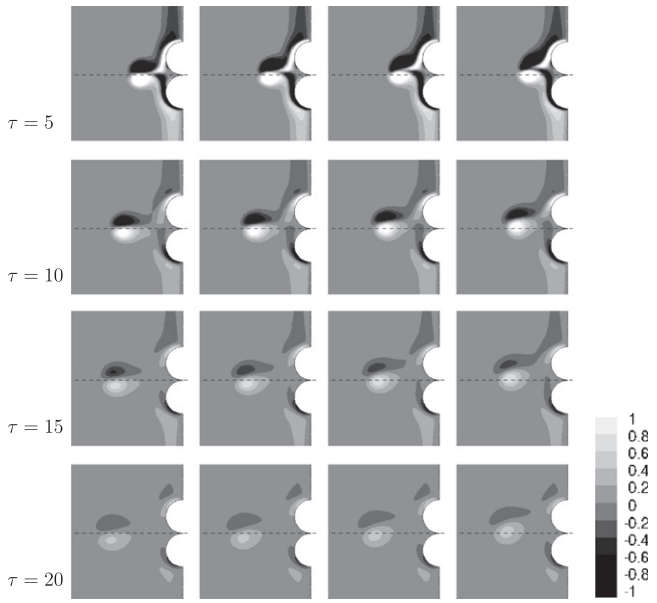

Fig. 6. Azimuthal vorticity plots for two equally sized spheres $D_t = D_b$ and for Re_b=400 and four different velocity ratios $U_t/U_b = \mathrm{Re}_t/\mathrm{Re}_b = 0.9$, 0.8, 0.7 and 0.6 (left to right), at times $\tau = tU_b/D_b = 5$, 10, 15 and 20 (the sphere on the top is traveling slower) (10 contour levels $-1U_b/D_b \le \omega_\theta \le 1U_b/D_b$).

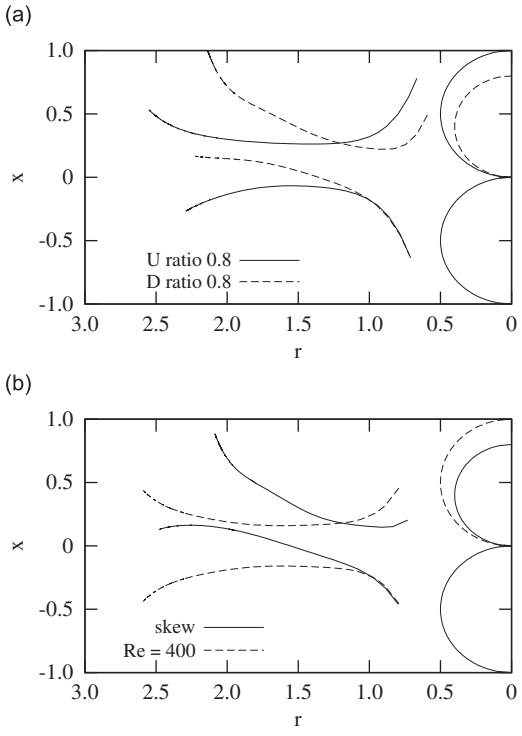

Fig. 7. (a) Trajectories of the two vortex ring cores formed for two collisions for Re_b=400, one case where the top sphere is traveling at $U_t = 0.8U_b$ (and $D_t = D_b$), the other with diameter $D_t = 0.8D_b$ (and $U_t = U_b$, then in both cases Re_t=320). (b) Trajectories of the two vortex ring cores formed for the symmetric collision for $\mathrm{Re}_t = \mathrm{Re}_b = 400$ and $D_t/D_b = U_t/D_b = 1$, the other where the top sphere is traveling at $U_t = 5/4U_b$ and with diameter $D_t = 4/5D_b$ such that $\mathrm{Re}_t = \mathrm{Re}_b = 400$. Spatial coordinates x and r are non-dimensionalized using D_b.

stronger vortex ring pushes the weaker one back across the midplane. The extent of the asymmetry of the flow increases with the difference in velocities. The stronger vortex ring strains the smaller one, elongating and pulling it around.

Fig. 7 plots vortex ring trajectories for various combinations of the parameters for the purpose of comparison. Fig. 7(a) compares two asymmetric cases, where the respective Reynolds numbers of each sphere differ, with Re_t=320 and Re_b=400.

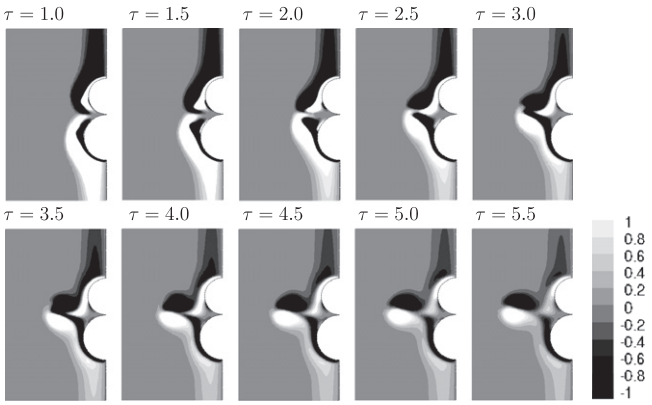

Fig. 8. Azimuthal vorticity contours of the flow after collision, with the upper sphere traveling at 0.8 of the velocity of the lower ($\mathrm{Re}_b = 400, U_t = U_b$, $D_t/D_b = \mathrm{Re}_t/\mathrm{Re}_b = 0.8$). The case corresponds to the dotted line case in Fig. 7(a).

In the first case, this difference results from different velocities, with $U_t/U_b = 0.8$ and $D_t/D_b = 1$ (also shown in Fig. 6), while in the second one it is due to different diameters, with $D_t/D_b = 0.8$ and $U_t/U_b = 1$. Therefore, considering our scaling equation for circulation, across both cases, the same difference in circulation generated exists, with the differences being in the geometries and the topology of the colliding vortex rings. In the case where the ratio of 0.8 pertains to the velocities, the resultant vortex rings emanate along, but just off, the midplane. Where the ratio pertains to the diameters, the vortex rings travel at a much greater angle from the midplane. Fig. 8 plots vorticity contours of the post-collision flow, corresponding to the $D_t/D_b = 0.8$ case of Fig. 7(a). One possible explanation of the difference in vortex ring trajectories is the effect of the secondary vorticity generated once the spheres are stopped. At times $2.5 < \tau < 4.0$, we observe that due to the imbalance of the collision, the secondary vorticity from the bottom sphere connects up with the primary vorticity ring from the top sphere. Another possible cause of the different trajectory may be the positioning of the vortices at the instant of collision. The vortex generated by the smaller sphere is of smaller radius than the vortex ring generated by the greater sphere. This results in the vortex expansion beginning at an angle towards the smaller sphere. The effect can be seen at $\tau = 2.0$ in Fig. 8. This dependence on the particular vorticity topology after collision may explain why the two cases of Fig. 7(a) do not exhibit the same vortex ring trajectories, even though the same relative difference in generated circulation exists in both cases.

Similarly, Fig. 7(b) plots two ostensibly similar cases where $\mathrm{Re}_t = \mathrm{Re}_b = 400$. The first is the symmetric case with $U_t/U_b = D_t/D_b = 1$ as discussed in the first part of this paper; while in the second "skewed" case, the velocity of the top sphere (in the plot) is increased to $U_t = 5/4U_b$ and, in order to get the same Reynolds number, the diameter decreased to $D_t = 4/5D_b$. Therefore, the two cases generate the same amount of circulation. However, from the vortex ring trajectories we see that the geometric effect of the smaller diameter causes the vortex rings to emanate at a large angle to the midplane.

4. Conclusions

Numerical simulations of symmetric collisions between two spheres have been compared to experimental visualizations, with good agreement achieved between the two sets of results. The post-collision flow consists of a pair of symmetric expanding vortex rings, which bears much similarity to and is consistent with the behaviour of colliding vortex rings. Numerical results have also been presented for unbalanced collisions. For this purpose, one sphere has been altered to have either a smaller diameter or a slower collision speed, both cases resulting in a lower Reynolds number. Also shown was the case of spheres having different velocities and diameters, but with equivalent products of velocity and diameter *UD*. These cases show that similarities in the circulation generated by each sphere from one case to the next do not necessarily result in the same post-collision flow. Cases where one sphere generated greater circulation than the other did not always result in the stronger vortex ring pulling the weaker around. In cases where one sphere was smaller, the expansion of the vortex rings begins in a trajectory angled away from the impact plane. Furthermore, the vorticity dynamics of an unbalanced collision can result in the sharing of primary and secondary vorticity between the two spheres, leading to a variety of post-collision vortex trajectories. The presence of the secondary vorticity and the initial angle of expansion appear to be points of difference when comparing to the vorticity dynamics resulting from the collision of two vortex rings, particularly in unbalanced collisions.

References

Davis, R.H., Serayssol, J.M., Hinch, E.J., 1986. The elastohydrodynamic collision of two spheres. J. Fluid Mech. 163, 479–497.
Eames, I., Dalziel, S.B., 2000. Dust resuspension by the flow around an impacting sphere. J. Fluid Mech. 403, 305–328.
Hirt, C., Amsden, A., Cook, J., 1974. An arbitrary lagrangian eulerian finite element method for all flow speeds. J. Comput. Phys. 14, 227–253.

Joseph, G.G., Zenit, R., Hunt, M.L., Rosenwinkel, A.M., 2001. Particle–wall collisions in a viscous fluid. J. Fluid Mech. 433, 329–436.
Leweke, T., Schouveiler, L., Thompson, M.C., Hourigan, K., 2008. Unsteady flow around impacting bluff bodies. J. Fluid Struct. 24, 1194–1203.
Leweke, T., Thompson, M.C., Hourigan, K., 2004. Vortex dynamics associated with the collision of a sphere with a wall. Phys. Fluids 16, L74.
Leweke, T., Thompson, M.C., Hourigan, K., 2006. Instability of the flow around an impacting sphere. J. Fluid Struct. 22, 961–971.
Morton, B.R., 1984. The generation and decay of vorticity. Geophys. Astrophys. Fluid Dyn. 28, 277–308.
Munro, R.J., Bethke, N., Dalziel, S.B., 2009. Sediment resuspension and erosion by vortex rings. Phys. Fluids 21, 046601.
Orlandi, P., Verzicco, R., 1993. Vortex rings impinging on walls: axisymmetric and three-dimensional simulations. J. Fluid Mech. 256, 615–646.
Shariff, K., Leonard, A., 1992. Vortex rings. Annu. Rev. Fluid Mech. 24, 235–279.
Thompson, M.C., Leweke, T., Hourigan, K., 2007. Sphere–wall collisions: vortex dynamics and stability. J. Fluid Mech. 575, 121–148.
Walker, J.D.A., Smith, C.R., Cerra, A.W., Doligalski, T.L., 1987. The impact of a vortex ring on a wall. J. Fluid Mech. 181, 99–140.
Yang, F.L., Hunt, M.L., 2006. Dynamics of particle–particle collisions in a viscous liquid. Phys. Fluids 18, 121506.